The Astrophysical Journal Letters, 902:L8 (8pp), 2020 October 10 https://doi.org/10.3847/2041-8213/abb8c5

Helium-rich Superluminous Supernovae from the Zwicky Transient Facility

Lin Yan[1], D. A. Perley[2], S. Schulze[3], R. Lunnan[4], J. Sollerman[4], K. De[5], Z. H. Chen[6], C. Fremling[5], A. Gal-Yam[3], K. Taggart[2], T.-W. Chen[4], I. Andreoni[5], E. C. Bellm[7], V. Cunningham[8], R. Dekany[1], D. A. Duev[9], C. Fransson[4], R. R. Laher[10], M. Hankins[5], A. Y. Q. Ho[5], J. E. Jencson[11], S. Kaye[1], S. R. Kulkarni[5], M. M. Kasliwal[5], V. Z. Golkhou[7,12], M. Graham[5], F. J. Masci[10], A. A. Miller[13,14], J. D. Neill[5], E. Ofek[3], M. Porter[1], P. Mróz[9], D. Reiley[1], R. Riddle[1], M. Rigault[15], B. Rusholme[10], D. L. Shupe[10], M. T. Soumagnac[3,16], R. Smith[1], L. Tartaglia[4], Y. Yao[5], and O. Yaron[3]

[1] The Caltech Optical Observatories, California Institute of Technology, Pasadena, CA 91125, USA; lyan@caltech.edu
[2] Astrophysics Research Institute, Liverpool John Moores University, 146 Brownlow Hill, Liverpool L3 5RF, UK
[3] Department of Particle Physics and Astrophysics, Weizmann Institute of Science, Rehovot 76100, Israel
[4] The Oskar Klein Centre, Department of Astronomy, Stockholm University, AlbaNova, SE-106 91 Stockholm, Sweden
[5] Division of Physics, Mathematics and Astronomy, California Institute of Technology, Pasadena, CA 91125, USA
[6] Physics Department and Tsinghua Center for Astrophysics (THCA), Tsinghua University, Beijing, 100084, People's Republic of China
[7] DIRAC Institute, Department of Astronomy, University of Washington, 3910 15th Avenue NE, Seattle, WA 98195, USA
[8] Department of Astronomy, University of Maryland, College Park, MD 20742, USA
[9] Division of Physics, Mathematics, and Astronomy, California Institute of Technology, Pasadena, CA 91125, USA
[10] IPAC, California Institute of Technology, 1200 E. California Boulevard, Pasadena, CA 91125, USA
[11] Steward Observatory, University of Arizona, 933 North Cherry Avenue, Tucson, AZ 85721-0065, USA
[12] The eScience Institute, University of Washington, Seattle, WA 98195, USA
[13] Center for Interdisciplinary Exploration and Research in Astrophysics and Department of Physics and Astronomy, Northwestern University, 1800 Sherman Avenue, Evanston, IL 60201, USA
[14] The Adler Planetarium, Chicago, IL 60605, USA
[15] Université Clermont Auvergne, CNRS/IN2P3, Laboratoire de Physique de Clermont, F-63000 Clermont-Ferrand, France
[16] Lawrence Berkeley National Laboratory, 1 Cyclotron Road, Berkeley, CA 94720, USA
Received 2020 June 23; revised 2020 August 19; accepted 2020 August 23; published 2020 October 7

Abstract

Helium is expected to be present in the massive ejecta of some hydrogen-poor superluminous supernovae (SLSN-I). However, until now only one event has been identified with He features in its photospheric spectra (PTF10hgi). We present the discovery of a new He-rich SLSN-I, ZTF19aawfbtg (SN2019hge), at $z = 0.0866$. This event has more than 10 optical spectra at phases from −41 to +103 days relative to the peak, most of which match well with that of PTF10hgi. Confirmation comes from a near-IR spectrum taken at +34 days, revealing He I features with P-Cygni profiles at 1.083 and 2.058 μm. Using the optical spectra of PTF10hgi and SN2019hge as templates, we examined 70 other SLSNe-I discovered by Zwicky Transient Facility in the first two years of operation and found five additional SLSNe-I with distinct He-features. The excitation of He I atoms in normal core-collapse supernovae requires nonthermal radiation, as proposed by previous studies. These He-rich events cannot be explained by the traditional ^{56}Ni mixing model because of their blue spectra, high peak luminosities, and long rise timescales. Magnetar models offer a possible solution since pulsar winds naturally generate high-energy particles, potential sources of nonthermal excitation. An alternative model is the interaction between the ejecta and dense H-poor circumstellar material, which may be supported by observed undulations in the light curves. These six SLSNe-Ib have relatively low-peak luminosities (rest frame $M_g = -20.06 \pm 0.16$).

Unified Astronomy Thesaurus concepts: Supernovae (1668); Type Ib supernovae (1729)

Supporting material: data behind figures

1. Introduction

Stars more massive than $\sim 8\,M_\odot$ end their lives as core-collapse supernovae (CC SNe; Jones et al. 2013). The observational properties of CC SNe are quite diverse, with much of this variety owing to variations in the mass-loss history of the progenitor stars. Hydrogen-rich CC SNe (Type II) result from massive stars that retain their hydrogen envelopes up until the time of explosion, and show hydrogen features in their spectra. Hydrogen-poor CC SNe (Type I) originate from massive stars that have lost most or all of their H envelopes prior to explosion. These include SNe IIb (some H and He), SNe Ib (no H, some He), and SNe Ic (no H, no He) (Filippenko 1997).

While it is not necessarily a surprise that helium is present within the envelopes of hydrogen-poor SN progenitors, the conditions necessary to produce observable helium features in SN spectra are not always easy to produce, and detections of helium in SNe Ib/IIb have motivated many theoretical calculations. For example, the He I λ5876 transition is between energy levels of $2p\ ^3P^0$ and $3d\ ^3D$. To reach these excited states from the ground state ($1s^2$) requires at least 20.9 eV of energy, corresponding to a temperature of $\sim 2.4 \times 10^5$ K. As noted by, e.g., Dessart et al. (2012) and Lucy (1991), γ-ray photons from ^{56}Ni decay can produce high-energy electrons via Compton scattering. These nonthermal electrons are a source of heat, critical for powering the light curve, as well as a source of nonthermal excitation and ionization for the production of optical He I lines observed in SNe Ib/IIb. This requires the transport of ^{56}Ni from the inner ejecta to the outer layer where helium material is located. Thus, the concept of the ^{56}Ni "mixing" is important for SNe Ib/IIb (Dessart et al. 2012).

Since the discovery of the first superluminous supernova (SLSN) more than 15 years ago (Quimby et al. 2007), more than 200 such events have been identified. A large fraction of low-z events are from two wide-area transient surveys: the Palomar Transient Factory (PTF; Law et al. 2009) and the Zwicky Transient Facility (ZTF; Graham et al. 2019; Bellm et al. 2019). SLSNe are 10–100 times more luminous than normal CC SNe and often maintain these luminosities for months, requiring additional power beyond what can be provided by the decay of radioactive material (Kasen & Bildsten 2010; Quimby et al. 2011; Yan et al. 2015; Woosley 2017). As with normal CC SNe, SLSNe are broadly categorized into two classes based on their spectrum around maximum light: hydrogen-poor (SLSN-I) and hydrogen-rich (SLSN-II) (Gal-Yam 2012).

Although hydrogen-poor SLSNe-I normally do not show hydrogen features in their spectra, a small fraction (∼10%–30%) show intermediate-width Hα emission (several thousand km s^{-1}) at >100 days post-peak, presumably produced by ejecta interaction with H-rich circumstellar material (CSM; Yan et al. 2015, 2017a). These cases suggest that the loss of the progenitor's hydrogen envelope must have occurred shortly before the explosions. The implication is that some helium is likely in the ejecta because there is not enough time to completely strip off all of the helium. However, SLSN-I spectral observations have not revealed the presence of helium, with one exception. Quimby et al. (2018) carried out a comprehensive spectral analysis of the entire PTF SLSN-I sample, and identified one event, PTF10hgi, with a clear detection of He I $\lambda\lambda$5876, 6678, 7065, and 7281 at ∼7000 km s^{-1}. This event also shows probable Hα with a broad P-Cygni profile with a velocity of 10,000 km s^{-1} at +47 days, suggesting that the event could be classified as an SLSN-IIb. The presence of Hα is further supported by a blended emission feature of [O I] λ6300 and Hα in the spectrum at +314 days. (SN2012il was proposed to have a He I 1.08μm feature by Inserra et al. 2013; however, Quimby et al. 2018 pointed out that this feature is unlikely to be He I, but may be broad nebular H emission.)

ZTF has been operating for over two years, and we have been systematically monitoring the data stream to search for and spectroscopically confirm new SLSNe, resulting in over 100 new SLSN discoveries to date (Lunnan et al. 2019; Z. Chen et al. 2020, in preparation) and a large accompanying spectral data set. Here we examine this data set, aiming to address if there are other He-rich SLSN-I similar to PTF10hgi. If such a population of events exists, further study of these events may shed light on the question of how helium atoms are excited and ionized, with important implications for the physical nature of SLSNe-I.

This Letter is organized as follows. Sections 2.1 and 2.2 present the optical and near-IR spectra for SN2019hge (ZTF19aawfbtg). Section 3 discusses the sample of SLSN-Ib/IIb events. The Letter concludes (Section 4) with a discussion of the key results and their implications. Throughout the Letter, all magnitudes are in the AB system unless explicitly noted otherwise. We adopt the ΛCDM cosmology with $H_0 = 67.4$ km s^{-1} Mpc^{-1}, $\Omega_M = 0.315$, and $\Omega_\Lambda = 0.685$ (Planck Collaboration et al. 2018).

Table 1
Optical Spectra for ZTF19aawfbtg[a]

Obs. Date	Phase[b] (days)	Tel/Instr	Exp. Time (s)	Δ λ (Å)	R[c]
2019-07-02	−26	Keck/LRIS	300	3100–10000	1000
2019-07-18	−12	P60/SEDM	1800	3900–9000	100
2019-07-26	−5	P60/SEDM	1800	3900–9000	100
2019-08-10	+9d	P60/SEDM	2250	3900–9000	100
2019-09-06	+33	P200/DBSP	900	3300–9800	956
2019-10-06	+61	P200/DBSP	900	3300–9800	956
2019-11-21	+103	Keck/LRIS	500	3900–9000	1000

Notes.
[a] All spectral observations were taken using parallactic angles.
[b] Phase is the rest-frame days from the g-band peak in the Julian date of 2,458,695.72.
[c] Spectral resolution R is estimated around 7000 Å.

2. Classification of SN2019hge (ZTF19aawfbgt) as an SLSN-Ib

2.1. Optical Spectra

Optical spectra of SN2019hge were obtained at −41 to +103 days from the g-band peak using the low-resolution ($R \sim 100$) Spectral Energy Distribution Machine (SEDM; Blagorodnova et al. 2018) and the Double Beam Spectrograph (DBSP; Oke & Gunn 1983) on the Palomar 60 inch and 200 inch telescopes, respectively, as well as the Low Resolution Imaging Spectrometer (LRIS; Oke et al. 1995) on the Keck I telescope. An observing log for all optical spectra of ZTF19aawfbtg presented here is in Table 1. Spectral reductions were performed using the SEDM pipeline and the *pyraf-dbsp* and *LPipe* packages (Rigault et al. 2019; Bellm & Sesar 2016; Perley 2019). Narrow Hα and [O II] λ3727 emission lines from the host galaxy establish the redshift as $z = 0.0866$. The supernova is at the edge of a face-on spiral galaxy with an estimated stellar mass of $\log_{10}(M_*/M_\odot) = 9.51^{+0.15}_{-0.29}$ from the spectral energy distribution (SED) fitting of broadband photometry provided by SDSS, PS1, 2MASS, and unWISE. This mass is larger than that of a typical SLSN-I host (Lunnan et al. 2014; Leloudas et al. 2015; Perley et al. 2016; Schulze et al. 2018).

We applied *Superfit* (Howell et al. 2013) with the enhanced SLSN spectral templates from Quimby et al. (2018) to our data. We find that for the spectra at phases later than −26 days, all five of the top matches returned by *Superfit* are with PTF10hgi. *Superfit*, like all spectral template matching software, can produce ambiguous classifications when the supernova features are weak. Thus, we also manually analyzed these spectra and established individual spectral line identifications. Figure 1 compares the spectra of SN2019hge with those of PTF10hgi and the low-luminosity Type Ib SN 2005bf (Folatelli et al. 2006). There are many similarities between these three events, in particular the four He I features at 5876, 6678, 7065, and 7281 Å blueshifted with a velocity of ∼7000 km s^{-1}. We do not consider He I $\lambda\lambda$3886, 4472 as the primary classification lines because of strong contamination from Ca II $\lambda\lambda$3934, 3969 (H+K lines) and Mg II λ4481. Of the four He features in Figure 1, He I λ5876 is strong with a well-defined absorption profile; however, it could have some contamination from

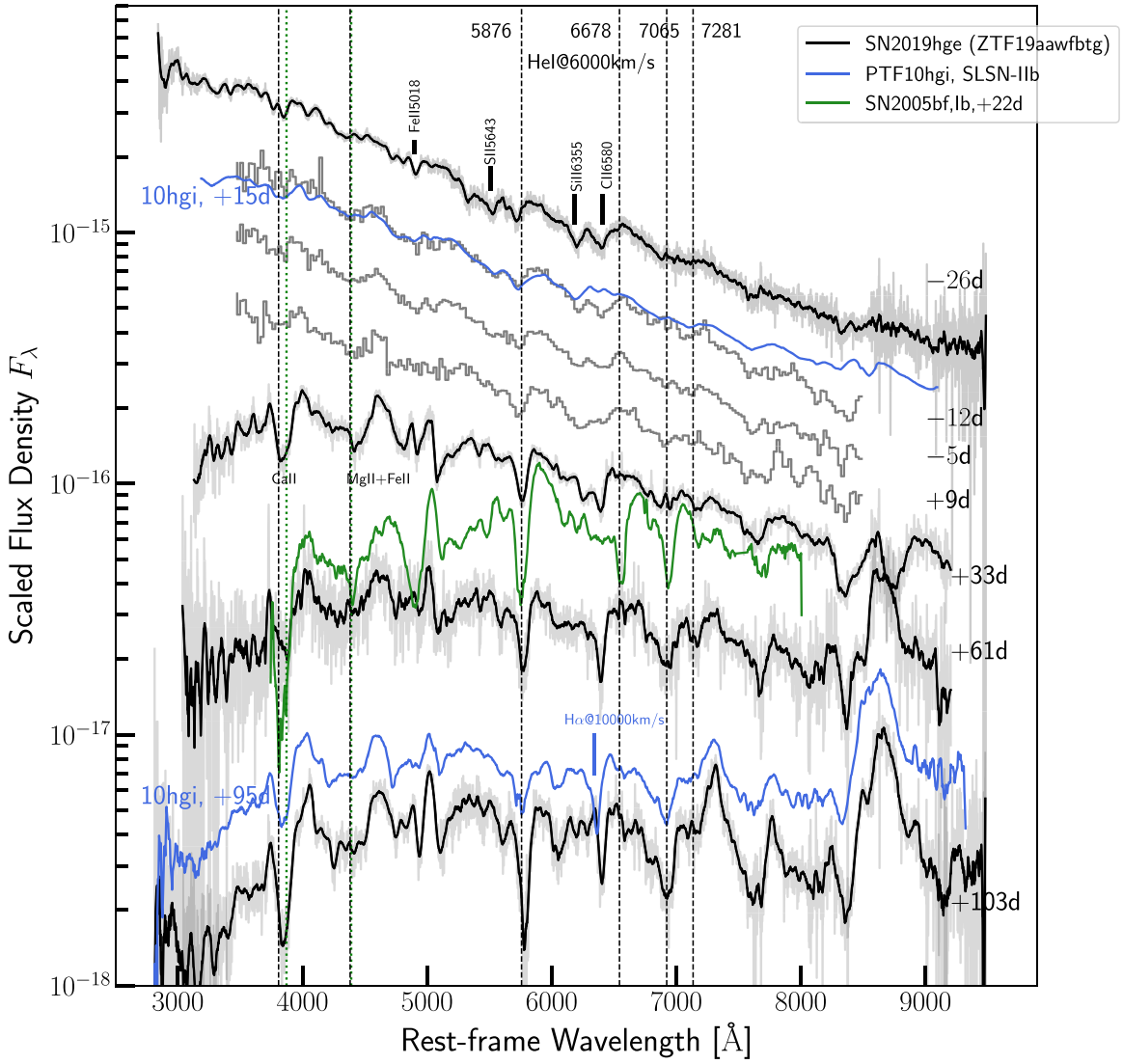

Figure 1. Spectra of SN2019hge (ZTF19aawfbtg) around peak and at late phases. Spectra of PTF10hgi (blue) and SN 2005bf (green) are also shown for comparison. The spectra shown in black are smoothed using the Savitzky–Golay filtering algorithm and overlaid onto the spectra in gray, which are the original data. The PTF10hgi and SN 2005bf spectra are also smoothed with the same method. The vertical dashed lines mark the locations of He I $\lambda\lambda$5876, 6678, 7065, and 7281 at a velocity of 7000 km s^{-1}.

(The data used to create this figure are available.)

Na I λ5890. The other three features are weak, but He I λ7065 is well isolated. Therefore, the key to identify He-rich events is the presence of multiple He features, as demonstrated in the classification of normal SNe Ib/IIb (Modjaz et al. 2014).

PTF10hgi has He I and Hα velocities of 7000 and 10,000 km s^{-1}, respectively, making it an SLSN-IIb (Quimby et al. 2018). In SN2019hge, hydrogen features are not as clear. In Figure 1, we marked the two features blueward of He I λ6678 as C II λ6580 and Si II λ6355. If these were Hα, the velocity would be either too low ($\sim$7800 km s^{-1}) or too high ($\sim$17,000 km s^{-1}). We thus conclude that SN2019hge is a H-poor and He-rich event. This classification was also noted by Prentice et al. (2019) reporting SN 2019hge as Type IIb based on their optical spectra.

2.2. Near-IR Spectral Confirmation of Helium in SN2019hge

SN2019hge was observed at +34 days with the Near-Infrared Echellette Spectrometer (NIRES; Wilson et al. 2004), a prism cross-dispersed near-infrared spectrograph mounted on the Keck II telescope. This spectrograph has a resolution of $\sim$2700 and simultaneously covers the *YJHK* bands with a wavelength range of 0.8–2.4 μm. The spectra were reduced with *Spextool* and *Xtellcor* written by Cushing et al. (2004) and Vacca et al. (2003). The data are shown in Figure 2, where the prominent feature at 1.08 μm is likely He I 1.08303 μm with the P-Cygni profile. This is confirmed by the presence of He I 2.05813 μm, a relatively isolated line. For comparison, we also plot the near-IR spectra of SN 2008ax, an SN IIb at −8 and +23 days from the *B*-band peak (Taubenberger et al. 2011). In Figure 2, we shift the spectra of SN 2008ax to a velocity of 6000 km s^{-1}. The match between SN2019hge and SN2008ax is very clear, including weak Mg I 1.1828, 1.2083 μm doublet. The relative strength of the 1.08 and 2.05μm features for SN2019hge is similar to that of SN2008ax at −8 days.

Assuming the minimum near 1.08μm is due to the P-Cygni profile of He I 1.08303 μm, the implied velocity is

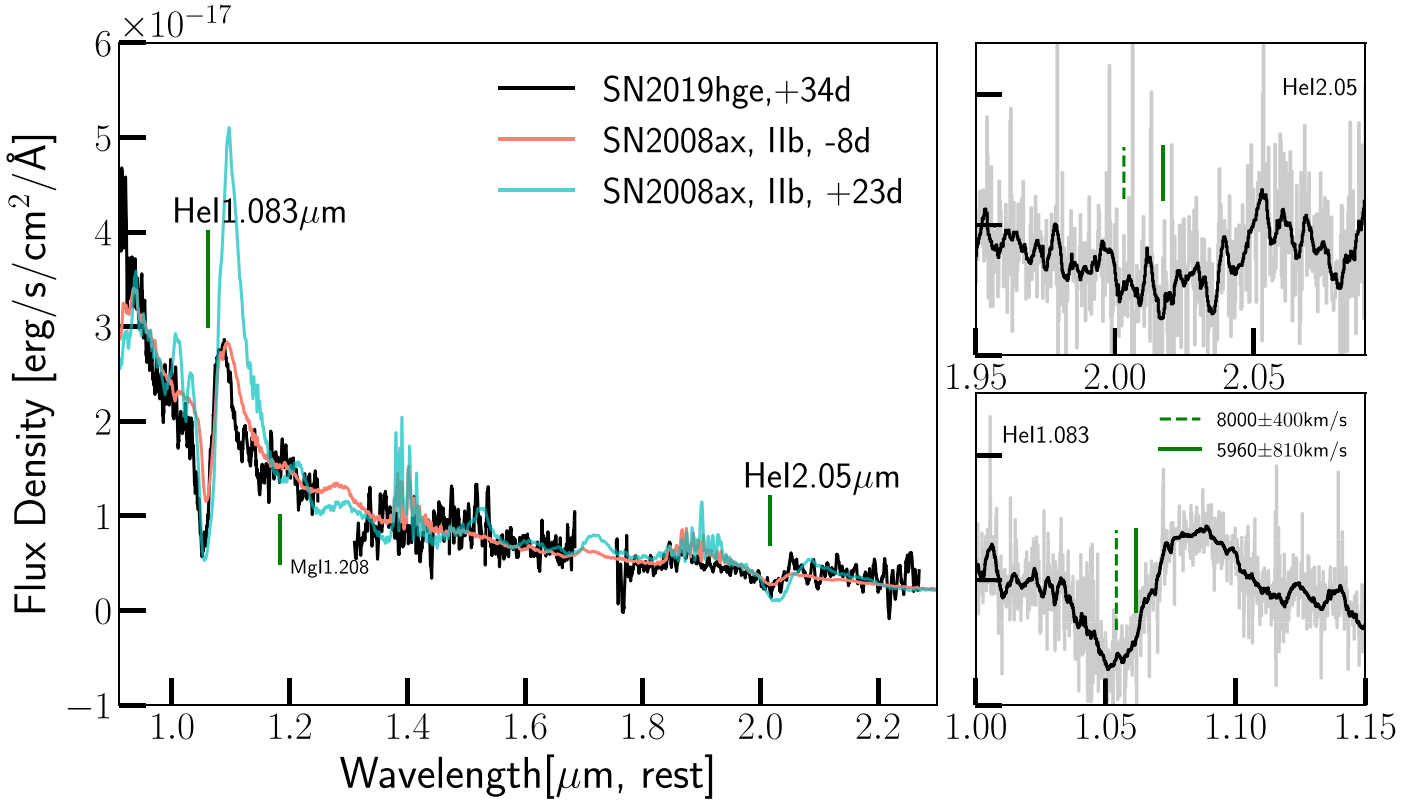

Figure 2. The near-IR spectrum of SN2019hge taken at +34 rest-frame days after the *g*-band peak date. The two panels on the right show the zoomed-in view of the two He I features. The gray spectra are original data, and the spectra in black have been smoothed using the Savitzky–Golay filtering algorithm. The vertical dashed and solid green lines mark two different blueshift velocities: 5960 km s^{-1} measured from the optical spectrum at +33 days, and 8000 km s^{-1}, which matches the minimum of the He I 1.083μm. The pink and cyan lines are the spectra of type IIb SN 2008ax (no smoothing) at −8 and +23 days from the *B*-band maximum light (Taubenberger et al. 2011). The SN 2008ax spectra are linearly shifted to match the velocity of 6000 km s^{-1} and no stretching was applied.

(The data used to create this figure are available.)

8000 km s^{-1}, as marked in green dashed vertical lines in the two right panels in Figure 2. Similarly, the He I 2.05813 μm P-Cygni profile gives a velocity of 6000 km s^{-1}, consistent with that derived from He I λ5876 at a similar phase of +33 day. It is possible that near-IR He I lines could have higher velocities than the optical He I lines because of their lower excitation. The lower velocity of He I λ2.058 μm could be due to its weaker and noisier feature. An alternative explanation is that He I 1.083 μm could be blended with C I 1.0691 μm at 6000 km s^{-1}, which would broaden and shift the minimum to shorter wavelengths. C I features are also present in the optical spectra at similar phases. The strong 1.08 μm features in normal SNe Ib/Ic could have contributions from He I, C I, Mg II, and Si I (Hunter et al. 2009; Taubenberger et al. 2011). However, unlike SNe Ib, normal SNe Ic do not have He I 2.058 μm (Taubenberger et al. 2011).

If hydrogen is present in the ejecta, Paγ at 1.0941 μm would imply a velocity of 11,000 km s^{-1}. Although this velocity is higher than expected, the presence of Paγ is not corroborated by Hα and Hβ in the optical spectra. In summary, the optical and near-IR spectra suggest that SN2019hge is a He-rich event.

3. A Sample of He-rich SLSN-I from ZTF

Assuming that optical spectra of PTF10hgi and SN2019hge can be used as templates to classify SLSN-Ib/IIb, we search for additional sources among the ZTF SLSNe-I discovered during the first two years of the survey. Figure 3 displays the spectra of six SLSNe-I, which are matched well with that of PTF10hgi, including SN2019hge. For these six ZTF events, their post-peak spectra are all matched with that of PTF10hgi among the top five ranks when we run *Superfit*. For each of the six events, at least three matches from *Superfit* are PTF10hgi at various phases, while the remaining one or two matches are other SLSN-I templates, such as PTF10nmn or PTF11rks. For example, for ZTF19acgjpgh, four out of five matches are PTF10hgi. All five matches are PTF10hgi for ZTF19aawfbtg.

Figure 3 compares these six events with PTF12dam (Quimby et al. 2018), an archetypal SLSN-I. Near $\lambda \sim 5876$ Å (He I), PTF12dam does not show a distinctive absorption feature, but a smooth and wide trough suggesting a blend of many lines. This is in contrast with the strong, narrow, and well-defined absorption features at 5876 Å detected in the six ZTF events. More importantly, three other He I lines at 6678, 7065, and 7281 Å are also present, albeit with various strengths. Considering that He-rich material in SN2019hge is confirmed by its near-IR spectrum, we conclude that the other five events are good SLSN-Ib/IIb candidates. In Figure 3, we note that SN2018kyt (ZTF18acyxnyw) may have Hα at $\sim$+10,000 km s^{-1}, a He-rich event with a potentially small amount of H, similar to PTF10hgi.

If the feature at 5876 Å is indeed blueshifted He I, we can measure the outflowing velocity V as well as the velocity dispersion by fitting a Gaussian profile to each feature. Figure 4 shows the He I velocities as a function of time. The velocities

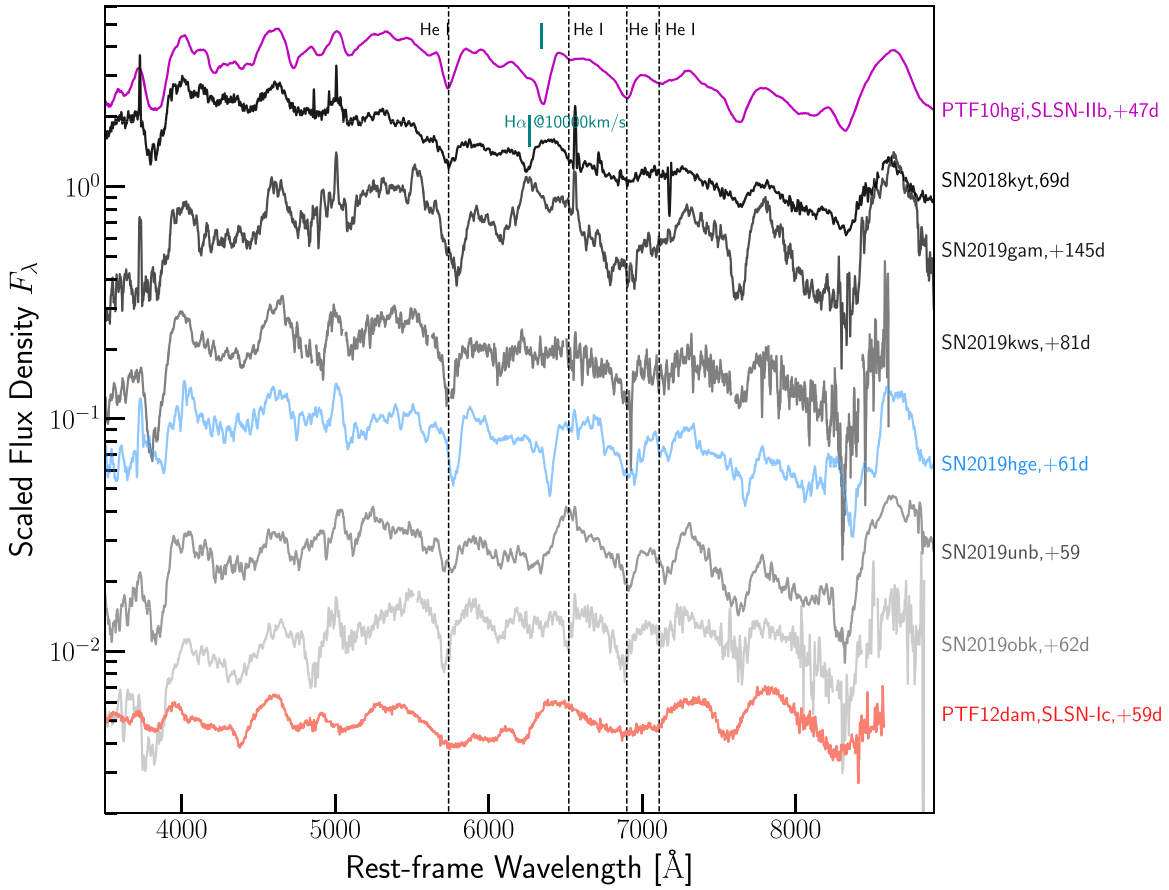

Figure 3. The post-peak spectra for a set of ZTF SLSNe-I are displayed in comparison with that of SN2019hge: PTF10hgi (an SLSN-IIb) and PTF12dam (an SLSN-I).

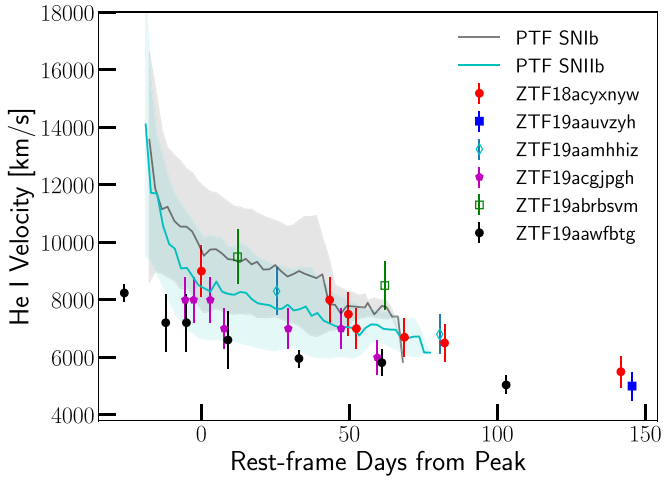

Figure 4. The outflowing velocity of He I λ5876 as a function of time measured for the six SLSNe-Ib/IIb.

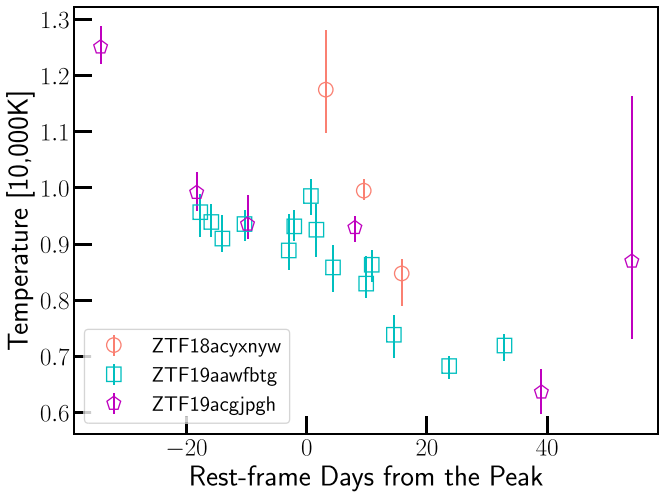

Figure 5. The modified blackbody temperatures measured from broadband photometry including one or more UV bands.

slow down roughly linearly with time, decreasing by 3000 km s^{-1} over 125 days. For comparison, Figure 4 also illustrates that the He I velocities in normal SNe Ib and IIb can drop from 14,000 km s^{-1} to 7000–6000 km s^{-1} in less than 90 days, a much more rapid evolution than what is seen in our He-rich SLSN-I sample. Finally, the He I line velocity dispersion, i.e., the line width, is ∼2000 km s^{-1} and remains roughly constant over the same period of time. This is much less than the bulk velocity, explaining the narrow appearance of the He I λ5876 line. Finally, Liu et al. (2016) found that for normal SNe Ib, their He I λ6676 and λ7065 lines have similar strength. This is not the case for our events, where the 6676 lines are on average weaker. This again suggests a different excitation mechanism from normal SNe Ib.

In addition, four of these six He-rich events have Swift UV photometry, and the blackbody temperatures are measured from fitting the broadband UV + optical spectral energy

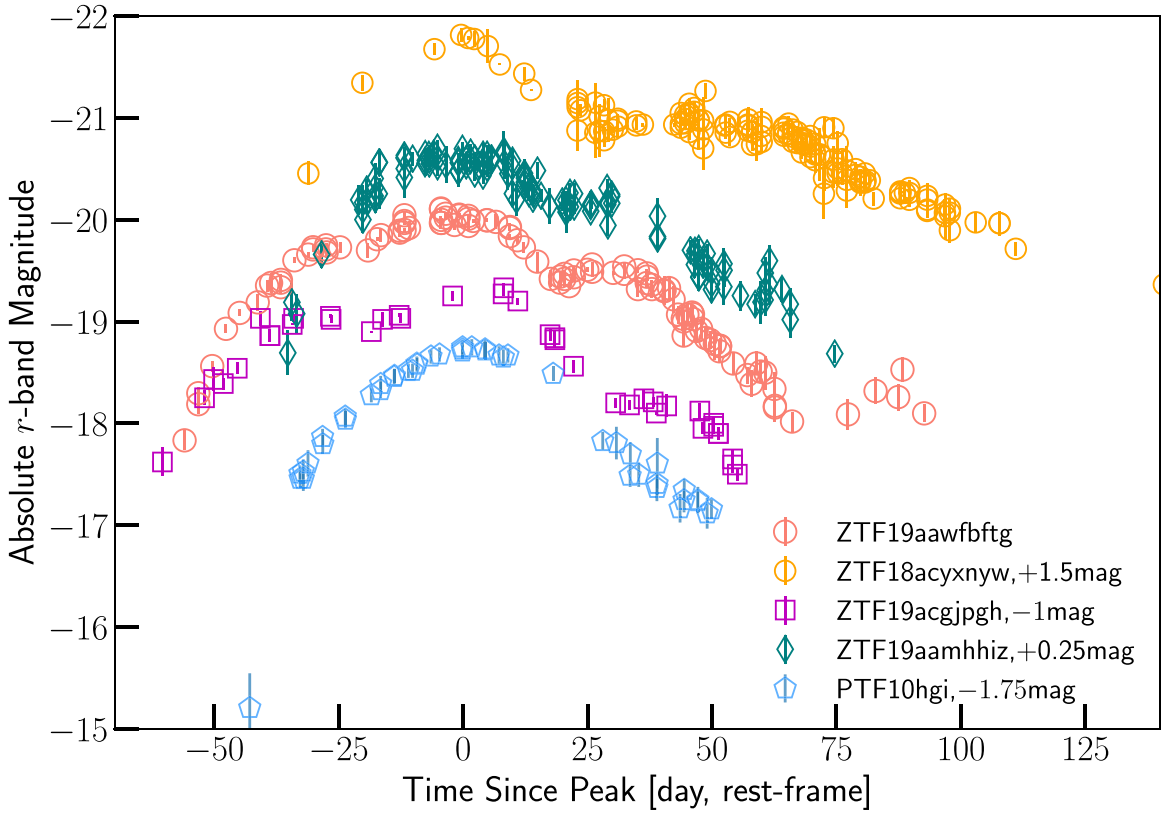

Figure 6. The r-band LCs of the five SLSNe-Ib whose LCs have good phase coverage.

distributions with a modified blackbody function of $B'_\lambda = \left(\frac{\lambda}{\lambda_0}\right)^\beta \times B_\lambda(T_{BB})$, where $\lambda_0 = 3000$ Å, and β and T_{BB} are derived from the fit (details in Z. Chen et al. 2020, in preparation). The rationale for this function is to take into account various degrees of SED suppression at far to near-UV due to metal line blanketing, as seen in the Hubble Space Telescope far-UV spectra of SLSN-I (Yan et al. 2017b; Yan et al. 2018). Figure 5 shows T_{BB} versus phases, illustrating that at pre-peak early phases, T_{BB} can reach as high as 12,000 K, commonly seen among SLSN-I (Quimby et al. 2011; Inserra et al. 2013; Chen et al. 2017; Nicholl et al. 2017). The He I features appear at phases when T_{BB} is a lower temperature, around ∼8000–7000 K.

Two outstanding features of this sample are shown by the light curves (LC) of the five events with good phase coverage from this sample, as in Figure 6. Here the LCs were constructed using the ZTF forced-photometry utility[17] and additional code from Yao et al. (2019) based on the reference subtracted images from the ZTF image reduction pipeline (Masci et al. 2019). The first notable feature is the prominent LC undulations in four of the six ZTF events (the other two have poor LC coverage). The physical interpretation of this behavior is not clear and there are multiple potential explanations, such as interaction or change in opacity. The second notable feature is the relatively low peak luminosity: all events are in the range of −19.8 to −20.2 absolute magnitude, for a sample of slow-evolving SLSNe-I with rising timescales of 35–68 days. Table 2 lists the name, coordinate, redshift (z), and g-band absolute peak magnitude (M_g). Extinction and K-corrections have been applied. This is in contrast to a much wider range of luminosity, −20 to −23 mag, normally occupied by SLSNe-I. Finally, we note that the host galaxies of these seven He-rich events include both low-mass dwarf galaxies and massive ones (10^9.5), but within the range expected for SLSNe-I (Lunnan et al. 2014; Perley et al. 2016; Schulze et al. 2018).

[17] http://web.ipac.caltech.edu/staff/fmasci/ztf/forcedphot.pdf

4. Discussion and Conclusions

The main result of this Letter is the discovery of a sample of He-rich SLSN-Ib/IIb, all of which are luminous (∼−20) and slow evolving with very large ejecta masses. Based on these six ZTF events, the percentage of He-rich events among ZTF SLSNe-I is ∼9%. This is just an observed fraction of SLSN-I. Detailed calculations of the volumetric rates including incompleteness are outside the scope of this Letter and will be discussed in a separate publication.

Helium is expected to be present in the ejecta of some massive stars if the stripping of the outer envelopes is incomplete. The detection of late-time, broad Hα emission in several PTF SLSNe-I (Yan et al. 2015, 2017a) has provided the first evidence that some massive stars lost their H-envelope shortly (<a few decades) before the supernova explosion, and never had enough time to also lose their helium layers. The fraction of SLSNe-I with late-time Hα emission is roughly 10%–30% (Yan et al. 2017a).

Our result has important implications for both the mass-loss history of progenitor stars as well as the power mechanism of SLSNe-I. Because the He I excitation energy is high, nonthermal excitation is required to produce observable helium features. For normal SNe Ib/IIb, nonthermal excitation is achieved by "mixing" that transports ^{56}Ni from the interior to the outer parts of ejecta (Lucy 1991; Dessart et al. 2012). This solution is unlikely to work for these SLSN-Ib because having

Table 2
A Sample of ZTF SLSN-Ib/IIb

Name	IAU Name	R.A.	Decl.	z	M_g
PTF10hgi	⋯	16:37:47.04	+06:12:32.3	0.0985	−20.2[a]
ZTF18acyxnyw	SN2018kyt	12:27:56.23	+56:23:35.6	0.108	−20.18
ZTF19aamhhiz	SN2019kws	14:15:04.46	+50:39:06.8	0.1977	−20.17
ZTF19aauvzyh	SN2019gam	10:19:18.32	+17:12:42.6	0.1235	…[b]
ZTF19aawfbtg	SN2019hge	22:24:21.20	+24:47:17.1	0.0866	−19.85
ZTF19acgjpgh	SN2019unb	09:47:57.02	+00:49:36.0	0.0635	−20.13
ZTF19abrbsvm	SN2019obk	22:33:54.08	−02:09:42.3	0.1656	−19.82

Notes.
[a] The number is from De Cia et al. (2018).
[b] No data within 100 days around the peak.

^{56}Ni as the sole power source would require extremely large ^{56}Ni masses, given the observed LCs with high peak luminosities and long rise timescales. Furthermore, Fe-group elements from ^{56}Ni decay will produce significant line blanketing in the UV/optical, leading to red spectra, in contrast to our observations (Figure 1). This argument also rules out the pair-instability supernova model (PISN; Woosley et al. 2007). For SLSNe-I, central engine models such as a magnetar or black hole fallback offer a natural source of high-energy particles from either pulsar wind or outflow from accretion disk. These outflow winds will interact with the inner regions of ejecta, producing shocks and X-rays. There are two spectral formation models for SLSN-I. One by Mazzali et al. (2016) assume X-rays from shocks driven by magnetar wind as a source of nonthermal excitation. The other by Dessart (2019) adopts a sustained magnetar energy injection profile (spatial). Both models are able to explain the hallmark O II absorption features at 3500–4500 Å (Quimby et al. 2011) and even produce He I λ5876 Å. However, both models do not deal with the dynamic processes of magnetar wind propagating through the ejecta. So the details of how magnetar energy is transported and thermalized to the outer layers are not understood. Furthermore, X-ray emission has not been detected from SLSNe-I (except one peculiar case) and current limits (Margutti et al. 2018) do not support the idea that shock interaction is an important energy source (Mazzali et al. 2016). The recent 3D magnetar simulation by Chen et al. (2020) has examined the dynamical processes, suggesting that Rayleigh–Taylor instability can quickly drive Ni and Fe to the outer layers. However, their work does not include simulated spectra. It is likely that Fe-group elements will make the spectra too red. Finally, ejecta–CSM interaction is a possible solution. The observed LC undulations from our sample may support this scenario. However, the LC undulations could also be related to the ejecta clumpiness and changes in opacity.

An important question is why only a small fraction of SLSN-I have He I features. Is the fraction of progenitors retaining some helium at the time of the explosion intrinsically small? If true, this would suggest very efficient mass-loss mechanisms. If massive stars are mostly in binaries, stripping by the secondary accretion is certainly more efficient than wind mass loss. An alternative scenario is that most SLSN-I progenitors have helium, but only a small fraction show He features in their spectra, either due to lack of excitation energy, or other peculiar physical conditions. Future modeling work may address this question.

Another spectral feature worth noting is that the early phase spectra of these events are blue continuum dominated without obvious O II absorption features (most notably, at −41 d for SN2019hge and −28 d for PTF10hgi). This cannot be explained by low temperatures: the early phase temperatures are clearly very high (Figure 5). Spectral smearing due to high velocity is also unlikely to provide a complete explanation because spectra taken post-peak all show narrow features with relatively low velocities (Figures 1 and 3). Like He I features, the formation of O II absorption requires not only sufficient excitation energy to produce ionized O^+, but also is affected by other factors, such as density and ionization parameter. However, the existing models have not provided clear physical explanations for why sometimes He I and O II absorption features are formed and sometimes they are not.

Based on observations obtained with the Samuel Oschin Telescope 48 inch and the 60 inch Telescope at the Palomar Observatory as part of the Zwicky Transient Facility project. ZTF is supported by the National Science Foundation under grant No. AST-1440341 and a collaboration including Caltech, IPAC, the Weizmann Institute for Science, the Oskar Klein Center at Stockholm University, the University of Maryland, the University of Washington, Deutsches Elektronen-Synchrotron and Humboldt University, Los Alamos National Laboratories, the TANGO Consortium of Taiwan, the University of Wisconsin at Milwaukee, and Lawrence Berkeley National Laboratories. Operations are conducted by COO, IPAC, and UW. The Liverpool Telescope is operated on the island of La Palma by Liverpool John Moores University in the Spanish Observatorio del Roque de los Muchachos of the Instituto de Astrofisica de Canarias with financial support from the UK Science and Technology Facilities Council. SED Machine is based upon work supported by the National Science Foundation under grant No. 1106171. The ZTF forced-photometry service was funded under the Heising-Simons Foundation grant #12540303 (PI: Graham). This work uses the GROWTH Followup Marshal (Kasliwal et al. 2019) and was supported by the GROWTH project funded by the National Science Foundation under grant No. 1545949. A.A.M. is funded by the Large Synoptic Survey Telescope Corporation, the Brinson Foundation, and the Moore Foundation in support of the LSSTC Data Science Fellowship Program; he also receives support as a CIERA Fellow by the CIERA Postdoctoral Fellowship Program (Center for Interdisciplinary Exploration and Research in Astrophysics, Northwestern University). R.L. is supported by a Marie Skłodowska-Curie Individual

Fellowship within the Horizon 2020 European Union (EU) Framework Programme for Research and Innovation (H2020-MSCA-IF-2017-794467).

ORCID iDs

Lin Yan https://orcid.org/0000-0003-1710-9339
D. A. Perley https://orcid.org/0000-0001-8472-1996
S. Schulze https://orcid.org/0000-0001-6797-1889
R. Lunnan https://orcid.org/0000-0001-9454-4639
J. Sollerman https://orcid.org/0000-0003-1546-6615
C. Fremling https://orcid.org/0000-0002-4223-103X
A. Gal-Yam https://orcid.org/0000-0002-3653-5598
I. Andreoni https://orcid.org/0000-0002-8977-1498
E. C. Bellm https://orcid.org/0000-0001-8018-5348
V. Cunningham https://orcid.org/0000-0003-2292-0441
R. Dekany https://orcid.org/0000-0002-5884-7867
D. A. Duev https://orcid.org/0000-0001-5060-8733
C. Fransson https://orcid.org/0000-0001-8532-3594
R. R. Laher https://orcid.org/0000-0003-2451-5482
M. Hankins https://orcid.org/0000-0001-9315-8437
A. Y. Q. Ho https://orcid.org/0000-0002-9017-3567
J. E. Jencson https://orcid.org/0000-0001-5754-4007
S. R. Kulkarni https://orcid.org/0000-0001-5390-8563
M. M. Kasliwal https://orcid.org/0000-0002-5619-4938
V. Z. Golkhou https://orcid.org/0000-0001-8205-2506
F. J. Masci https://orcid.org/0000-0002-8532-9395
A. A. Miller https://orcid.org/0000-0001-9515-478X
E. Ofek https://orcid.org/0000-0002-6786-8774
R. Riddle https://orcid.org/0000-0002-0387-370X
M. Rigault https://orcid.org/0000-0002-8121-2560
B. Rusholme https://orcid.org/0000-0001-7648-4142
D. L. Shupe https://orcid.org/0000-0003-4401-0430
M. T. Soumagnac https://orcid.org/0000-0001-6753-1488
L. Tartaglia https://orcid.org/0000-0003-3433-1492

References

Bellm, E. C., Kulkarni, S. R., Graham, M. J., et al. 2019, PASP, 131, 018002
Bellm, E. C., & Sesar, B. 2016, pyraf-dbsp: Reduction pipeline for the Palomar Double Beam Spectrograph, Astrophysics Source Code Library, ascl:1602.002
Blagorodnova, N., Neill, J. D., Walters, R., et al. 2018, PASP, 130, 035003
Chen, K.-J., Woosley, S. E., & Whalen, D. J. 2020, ApJ, 893, 99
Chen, T. W., Nicholl, M., Smartt, S. J., et al. 2017, A&A, 602, A9
Cushing, M. C., Vacca, W. D., & Rayner, J. T. 2004, PASP, 116, 362
De Cia, A., Gal-Yam, A., Rubin, A., et al. 2018, ApJ, 860, 100
Dessart, L. 2019, A&A, 621, A141
Dessart, L., Hillier, D. J., Waldman, R., et al. 2012, MNRAS, 426, L76
Filippenko, A. 1997, ARA&A, 35, 309
Folatelli, G., Contreras, C., Phillips, M. M., et al. 2006, ApJ, 641, 1039
Gal-Yam, A. 2012, Sci, 337, 927
Graham, M. J., Kulkarni, S. R., Bellm, E. C., et al. 2019, PASP, 131, 078001
Howell, D. A., Kasen, D., Lidman, C., et al. 2013, ApJ, 779, 98
Hunter, D. J., Valenti, S., Kotak, R., et al. 2009, A&A, 508, 371
Inserra, C., Smartt, S., Jerkstrand, A., et al. 2013, ApJ, 770, 128
Jones, S., Hirschi, R., Nomoto, K., et al. 2013, ApJ, 772, 150
Kasen, D., & Bildsten, L. 2010, ApJ, 717, 245
Kasliwal, M. M., Cannella, C., Bagdasaryan, A., et al. 2019, PASP, 131, 038003
Law, N. M., Kulkarni, S. R., Dekany, R. G., et al. 2009, PASP, 121, 1395
Leloudas, G., Schulze, S., Krühler, T., et al. 2015, MNRAS, 449, 917
Liu, Y.-Q., Modjaz, M., Bianco, F. B., & Graur, O. 2016, ApJ, 827, 90
Lucy, L. B. 1991, ApJ, 383, 308
Lunnan, R., Chornock, R., Berger, E., et al. 2014, ApJ, 787, 138
Lunnan, R., Yan, L., Perley, D. A., et al. 2019, arXiv:1910.02968
Margutti, R., Chornock, R., Metzger, B. D., et al. 2018, ApJ, 864, 45
Masci, F. J., Laher, R. R., Rusholme, B., et al. 2019, PASP, 131, 018003
Mazzali, P. A., Sullivan, M., Pian, E., et al. 2016, MNRAS, 458, 3455
Modjaz, M., Blondin, S., Kirshner, R. P., et al. 2014, AJ, 147, 99
Nicholl, M., Berger, E., Margutti, R., et al. 2017, ApJL, 845, L8
Oke, J. B., Cohen, J. G., Carr, M., et al. 1995, PASP, 107, 375
Oke, J. B., & Gunn, J. E. 1983, ApJ, 266, 713
Perley, D. A. 2019, PASP, 131, 084503
Perley, D. A., Quimby, R. M., Yan, L., et al. 2016, ApJ, 830, 13
Planck Collaboration, Aghanim, N., Akrami, Y., et al. 2018, arXiv:1807.06209
Prentice, S. J., Maguire, K., Skillen, K., et al. 2019, TNSAN, 74, 1
Quimby, R. M., Aldering, G., Wheeler, J. C., et al. 2007, ApJL, 668, L99
Quimby, R. M., De Cia, A., Gal-Yam, A., et al. 2018, ApJ, 855, 2
Quimby, R. M., Kulkarni, S. R., Kasliwal, M. M., et al. 2011, Natur, 474, 487
Rigault, M., Neill, J. D., Blagorodnova, N., et al. 2019, A&A, 627, A115
Schulze, S., Krühler, T., Leloudas, G., et al. 2018, MNRAS, 473, 1258
Taubenberger, S., Navasardyan, H., Maurer, J. I., et al. 2011, MNRAS, 413, 2140
Vacca, W. D., Cushing, M. C., & Rayner, J. T. 2003, PASP, 115, 389
Wilson, J. C., Henderson, C. P., Herter, T. L., et al. 2004, Proc. SPIE, 5492, 1295
Woosley, S. E. 2017, ApJ, 836, 244
Woosley, S. E., Blinnikov, S., & Heger, A. 2007, Natur, 450, 390
Yan, L., Lunnan, R., Perley, D. A., et al. 2017a, ApJ, 848, 6
Yan, L., Perley, D. A., De Cia, A., et al. 2018, ApJ, 858, 91
Yan, L., Quimby, R., Gal-Yam, A., et al. 2017b, ApJ, 840, 57
Yan, L., Quimby, R., Ofek, E., et al. 2015, ApJ, 814, 108
Yao, Y., Miller, A. A., Kulkarni, S. R., et al. 2019, ApJ, 886, 152